Optics and Lasers in Engineering 178 (2024) 108191

Contents lists available at ScienceDirect

Optics and Lasers in Engineering

journal homepage: www.elsevier.com/locate/optlaseng

Mueller-Gabor holographic microscopy

Maria J. Lopera [a,b,*], Maciej Trusiak [c], Ana Doblas [d], Heidi Ottevaere [a], Carlos Trujillo [b]

[a] Brussels Photonics, Department of Applied Physics and Photonics, Vrije Universiteit Brussel and Flanders Make, Pleinlaan 2, B-1050 Brussels, Belgium
[b] Applied Optics Group, School of Applied Science and Engineering, Universidad EAFIT, Medellín, Colombia
[c] Warsaw University of Technology, Institute of Micromechanics and Photonics, 8 Sw. A. Boboli St., 02-525 Warsaw, Poland
[d] ECE Department, University of Massachusetts Dartmouth, New Bedford, MA 02747, USA

ARTICLE INFO

Keywords:
In-line holography
Gabor holography
Mueller matrix
Polarization-sensitive

ABSTRACT

Despite the emergence of various methods for Mueller matrix recovery, achieving complete volumetric Mueller matrix retrieval remains a challenge. An alternative approach that leverages in-line Gabor holography to comprehensively extract polarization information from volumetric samples is introduced in this context. The proposed polarization-sensitive in-line Gabor holographic setup enables the recovery of the complete Mueller matrix of three-dimensional (3D) samples after the numerical repropagation of the holographically rendered complex field to various sample planes. This proposal is validated using a calibrated birefringent polarization test target, a sample of Calcium Oxalate crystals, and a volumetric sample containing microplastics, providing the 3D measurement of polarimetric parameters such as diattenuation, polarizance, depolarization, and retardance. The results agree with those obtained through reference methods based on image-plane brightfield polarimetry. The in-line Gabor holographic system proposed is sensitive to the axial variations in polarimetric information within volumetric samples without any mechanical movement nor optical adjustments— an accomplishment that remains elusive to conventional image-plane reference methods and non-holographic/interferometric systems. These findings emphasize the versatility and potential of this alternative approach in recovering the intricate polarization characteristics of 3D specimens, offering the first in-line holographic Mueller imaging to the best of the authors' knowledge.

1. Introduction

The computation of the Mueller matrix, which characterizes the polarization properties of light interacting with a sample, holds immense significance across various scientific domains, particularly in biology and medicine [1–5]. Understanding and quantifying the polarization behavior of samples is pivotal for applications such as tissue characterization [6–8], early cancer detection [9], diagnostics of painful disorders [10], and the study of structural properties in biological specimens [11,12], to name some of them. The Mueller matrix (MM) comprehensively describes how light polarization is modified upon interaction with a sample, providing crucial insights into the sample's structural and optical properties in various imaging modalities apart from the conventional amplitude and phase imaging. For this reason, the accurate retrieval of this information has become indispensable for researchers and practitioners aiming to harness polarimetry's potential for enhancing the accuracy and sensitivity of diagnostics and investigations in biology and medicine.

The recovery of the MM has relied on various polarimetric techniques, such as rotating waveplates, polarization modulators, swept sources, and a combination of retarders and polarizers [13–16]. These methods involve altering the polarization state of incident light and measuring the resulting intensity changes to derive individual matrix elements [17–19]. The major limitation of these conventional MM-based techniques is that they are restricted to single-image-plane measurements (i.e., 2D), limiting their ability to capture volumetric polarization information. Although different approaches have been proposed to compensate for this drawback, bulky and expensive setups have been required [20]. Mueller matrix imaging has recently been introduced to the field of 3D integral imaging [21]. In this approach, a conventional three-dimensional (3D) integral system is modified to obtain polarimetric measurements at the expense of an increased computational complexity and intricate sample preparation process.

In the Digital Holography (DH) field, significant advancements have

* Corresponding author.
E-mail addresses: mloper23@eafit.edu.co, maria.josef.lopera.acosta@vub.be (M.J. Lopera), maciej.trusiak@pw.edu.pl (M. Trusiak), adoblas@umassd.edu (A. Doblas), heidi.ottevaere@vub.be (H. Ottevaere), catrujilla@eafit.edu.co (C. Trujillo).

https://doi.org/10.1016/j.optlaseng.2024.108191
Received 23 October 2023; Received in revised form 5 February 2024; Accepted 12 March 2024
Available online 21 March 2024

been made in polarization-sensitive techniques[14]. In 2002, Colomb et al. [22] pioneered the simultaneous determination of intensity, phase, and polarization state using two orthogonal reference waves. In their approach, the authors record holograms on a CCD camera using a modified Mach Zehnder-based DH system to reconstruct two wavefronts, allowing the Jones vector components to be determined. Subsequently, using the same DH system and additional polarization elements, they introduce a digital holographic microscope capable of imaging polarization states and measured phase differences in birefringence [23]. In [24], traditional holographic techniques study birefringence and dichroism in anisotropic samples. In [25], an extension of the MM formalism is introduced for scattered light, resulting in an MM holography method for obtaining complete polarization information, particularly suitable for studying anisotropic particles. Regarding the explicit measurement of the MM, a digital holographic off-axis Mueller matrix imaging method has been proposed [26], providing 3D MM imaging from 12 recordings, assuming poor polarization response to circular light, and reporting errors of 23 % on average. In [27], the authors extend the idea of microsphere-assisted microscopy into Mueller matrix microscopy toward resolution-enhanced polarimetric imaging. The insertion of a transparent microsphere in the working distance of the imaging microscope objective in the optical train of the imaging system achieves the goal. More recently, a polarization-holographic Mueller matrix method has been reported to assess the 3D morphology with applications for medical diagnosis using specialized diffuse layers of polyvinyl acetate in the interferometric system [28]. It is important to note that all these DH approaches for 3D Mueller matrix retrieval either demand robust interferometric setups, specialized optical elements, or intensive computational stages, thereby limiting the scope of their application.

Despite the successful performance of MM-based imaging systems, their applicability to in situ clinical research has been hampered by the need for a simple imaging technique that retrieves the polarimetric parameters (i.e., diattenuation, polarizance, depolarization, and retardance) of 3D samples. This study proposes a Mueller Gabor holography microscopy (MG-HM) method as an alternative approach to address the challenge of obtaining comprehensive polarization information from volumetric samples. As with any other DH implementation, in-line Gabor holography [29–32] enables refocusing the reconstructed defocused image, therefore attaining the complex amplitude-phase field of the optimal focal plane through numerical propagation algorithms [33]. This means that in-line Gabor holography allows the visualization of the sample under various imaging modalities, including amplitude, dark-field, intensity, or phase reconstructions, and at different object depths. This research study introduces and demonstrates the application of this MG-HM technique to tackle the challenge of retrieving comprehensive polarization information from volumetric samples. The capabilities of in-line Gabor holography with polarization sensitivity are integrated to achieve this. This alternative approach effectively allows recovering the complete MM using simple hardware requiring an illumination source, conventional polarimetric elements, a microscope objective, and a digital camera. The experimental results show the potential and versatility of the technique proposed here as a 3D polarimeter.

This paper is structured as follows. Section 2 presents the fundamentals of the proposed method. Section 3 provides comprehensive experimental validation, measuring the MM of a calibrated polarization test target, a sample containing Calcium Oxalate crystals, and a volumetric sample containing microplastics. Section 4 analyzes the full potential of the polarization-sensitive in-line Gabor DH system for studying volumetric samples. Finally, the paper concludes with a summary of findings and conclusions.

2. Gabor holography and mueller matrix retrieval fundamentals

The proposed method for recovering the MM combines the elements of an in-line Gabor holographic setup [29] with a conventional polarimetric configuration [13], as depicted in Fig. 1. The Mueller-Gabor Holographic Microscopy (MG-HM) setup uses a linearly polarized laser source ($\lambda = 532$ nm). The emerging linearly polarized light is expanded and spatially filtered to produce a cleaner and larger beam spot of 2.5 ± 0.1 mm. A Polarization States Generator (PSG), consisting of a half-wave (i.e., $\lambda/2$) and quarter-wave (i.e., $\lambda/4$) plate, is inserted before the microscopic sample to have precise control of the incident illuminating polarization state. The sample's information is represented by a complex wavefield $S(\overrightarrow{r_0})$ where $\overrightarrow{r_0}$ is the position vector. A non-infinity-corrected microscope objective (MO) lens is inserted after the sample, creating a focused and magnified image of the sample's information, $S(\overrightarrow{r_i}) = (1/|M|)\cdot S(\overrightarrow{r_0}/M)$ where M is the lateral magnification provided by the MO lens and $\overrightarrow{r_i}$ is the position vector at the image plane located at a distance f_0 from the rear face of the MO. The theoretical lateral resolution of the optical setup depends upon the numerical aperture of the imaging system (following the Abbe's principle) and the discretization on the sensor plane (following the Nyquist principle) [34]. A Polarization State Analyzer (PSA) is inserted between the MO lens and the image plane to process the modified polarization state of the outgoing light as it interacts with the sample before reaching the sensor. The PSA comprises a quarter-wave plate ($\lambda/4$) followed by a linear polarizer (LP). The sensor's plane is positioned at a distance z from the image plane to record a defocused intensity image of the sample, leveraging the principles of in-line Gabor holography [29].

After recording $I_d(\overrightarrow{r_i}, z)$, the information of the wavefield scattered by the sample $S(\overrightarrow{r_i})$, can be recovered within an inspection volume on a plane-by-plane basis [33,35,36]. Numerical processing of the recorded hologram is required to recover this wavefield by backpropagating this intensity from the sensor to the image plane to get the in-focus sample distribution, $S(\overrightarrow{r_i})$. A classical approach is to use the Angular Spectrum formalism (AS) [33,37,38] to recover this information via $S(\overrightarrow{r_i}) = \mathrm{AS}\{I_d(\overrightarrow{r_i}, z)\}$. This process results in the reconstruction of the image plane's intensity, $I(\overrightarrow{r_i}) = |S(\overrightarrow{r_i})|^2$, which is later utilized to compute the MM of the sample.

A series of 36 in-line holograms are captured by systematically adjusting the configurations of PSG and PSA to pointwise recover the MM of the studied sample. The intensity reconstruction at the selected sample's plane (within the measured volume of interest) is calculated for each hologram. Following a methodology analogous to conventional polarization microscopy [15], these 36 intensity reconstructions are then employed to recover the complete MM of the sample, which is defined by Eq. (1).

$$M_u(\overrightarrow{r_i}\cdot M) = \begin{bmatrix} m_{00} & m_{01} & m_{02} & m_{03} \\ m_{10} & m_{11} & m_{12} & m_{13} \\ m_{20} & m_{21} & m_{22} & m_{23} \\ m_{30} & m_{31} & m_{32} & m_{33} \end{bmatrix} \tag{1}$$

Each element of the MM, m_{ij}, is calculated through a point-by-point addition or subtraction of four intensity reconstructions, as specified in Equations (2). This means that each m_{ij} element is a 2D map (i.e., matrix). In Eq. (2), the first letter indicates the polarization state of the PSG system, while the second letter corresponds to the polarization state of the PSA system. For instance, the element m_{00} is determined by combining the intensity reconstructions of *HH, HV, VH*, and *VV*. Note that 'H' represents a linearly horizontal polarization state, 'V' denotes the linearly vertical polarization state, and 'P' and 'M' represents the linearly polarization state oriented at $+45$ and $-45°$, respectively. The circular polarization states are denoted by 'R' for the right-handed orientation and 'L' for the left-handed one. For example, the '*HH*' intensity reconstruction denotes horizontal linear polarization for both the PSG and PSA systems. Appendix A provides the configuration of the PSG and PSA systems to obtain the polarization states during the hologram recording. One of the advantages of this method is that the MM can be completely recovered by solving a system of linear equations without

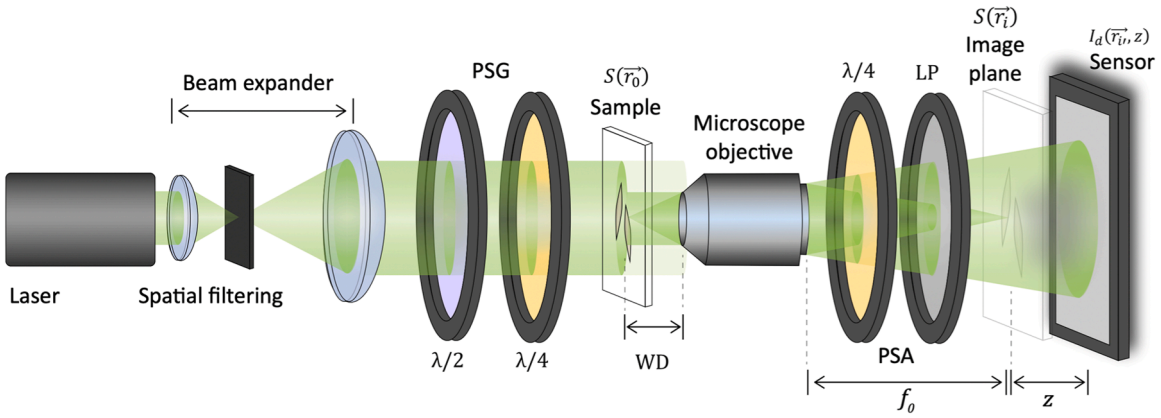

Fig. 1. Scheme of the proposed MG-HM setup.

any assumptions and/or approximations [17].

$$\begin{aligned} m_{00} &= HH + HV + VH + VV & m_{01} &= HH + HV - VH - VV \\ m_{02} &= PP + PV - MH - MV & m_{03} &= RH + RV - LH - LV \\ m_{10} &= HH - HV + VH - VV & m_{11} &= HH - HV - VH + VV \\ m_{12} &= PH - PV - MH + MV & m_{13} &= RH - RV - LH + LV \\ m_{20} &= HP - HM + VP - VM & m_{21} &= HP - HM - VP + VM \\ m_{22} &= PP - PM - MP + MM & m_{23} &= RP - RM - LP + LM \\ m_{30} &= HR - HL + VR - VL & m_{31} &= HR - HL - VR + VL \\ m_{32} &= PR - PL - MR + ML & m_{33} &= LL - RL - LR + RR \end{aligned} \tag{2}$$

After the Mueller matrix is obtained, the following polarimetric parameters (among others) can be computed [15,17,18]

$$\textbf{\textit{Diattenuation}}\ (\boldsymbol{D})D = \frac{\sqrt{\boldsymbol{m}_{01}^2 + \boldsymbol{m}_{02}^2 + \boldsymbol{m}_{03}^2}}{\boldsymbol{m}_{00}} \tag{3}$$

$$\textbf{\textit{Polarizance}}\ (\boldsymbol{P})\boldsymbol{P} = \frac{\sqrt{\boldsymbol{m}_{10}^2 + \boldsymbol{m}_{20}^2 + \boldsymbol{m}_{30}^2}}{\boldsymbol{m}_{00}} \tag{4}$$

$$\textbf{\textit{Depolarization}}\ (\Delta)\Delta = 1 - \frac{\sqrt{\left(\sum_{i=1}^{3} \boldsymbol{m}_{ii}^2\right) - \boldsymbol{m}_{00}^2}}{\sqrt{3}\ \boldsymbol{m}_{00}} \tag{5}$$

$$\textbf{\textit{Linear dichroism}}\ (\boldsymbol{LD})LD = \frac{HH - HV}{HH + HV} \tag{6}$$

$$\textbf{\textit{Retardance}}\ (\boldsymbol{R})R = \cos^{-1}\left(\mathrm{Tr}\left(\frac{\mathrm{M_R}}{2}\right) - 1\right) \tag{7}$$

Eqs. (3)-(7) provide quantitative measurements for the respective polarimetric properties of samples, offering valuable insights into the sample's optical polarization-state-altering characteristics [15]. Specifically, the retardance is computed from the polar decomposition of the MM, obtaining the trace (Tr) of the retardance Mueller matrix ($\mathrm{M_R}$), described by [18], and detailed in Appendix A. By computing these properties, researchers can comprehensively understand how the sample interacts with polarized light, making it applicable in diverse fields, such as multi-domain imaging for material science and biomedical research [8,26,35,39].

The following steps delineate the procedure for extracting the MM of the sample in this proposal.

2.1. Hologram acquisition

a. Configure the PSG elements to various combinations of angles to generate a set of incident polarization states. Refer to Appendix A for the necessary PSG combinations.
b. Maintain the PSG settings and adjust the PSA elements to capture images featuring distinct outgoing polarization states. Appendix A contains the required PSA combinations.
c. Record a Gabor hologram for each incident and outgoing polarization state combination, ensuring the sample's position and the z distance remain unchanged.

In this proposal, the adjustment of both the PSG and PSA has been executed manually. The manual adjustment introduces variability in the acquisition speed of the holograms, which is inherently dependent on the researcher's expertise during the implementation of the method. Nonetheless, the proposed method can be performed digitally if the polarizing elements are mounted on rotational mounts, reducing the acquisition time.

2.2. Intensity reconstruction

a. Employ the Angular Spectrum formalism to propagate each recorded Gabor hologram back to the original sample image plane.
b. Calculate the intensity ($|S(\vec{r_0}/M)|^2$) distribution from the reconstructed complex wavefields for each combination of incident and outgoing polarization states.
c. Normalize each reconstructed intensity and scale it by a factor equivalent to the initial hologram intensity. This factor is determined by calculating the sum of the intensities across all 36 holograms and then finding the maximum intensity value within this dataset. Subsequently, each hologram's intensity is scaled by the ratio of its own intensity to the maximum intensity found. This process guarantees that the relative intensity of each recording is maintained intact throughout the numerical processing of the holograms.

2.3. Mueller matrix calculation

After acquiring the set of 36 normalized and scaled intensity-reconstructed images, calculate each element of the MM individually, following Eqs. (2) and (3).

3. Experimental validation of the polarization-sensitive in-line gabor system

To validate the capacity of the proposed in-line Gabor holographic system to obtain accurate quantitative measurements of the polarization response, a birefringent resolution target (Thorlabs R2L2S1B) is employed. This target comprises a birefringent pattern sandwiched between a glass substrate and protective glass (N-BK7). This target is only observable when placed between a pair of crossed polarizers. The experimental details of MG-HM setup are outlined in Appendix B to image the birefringent resolution target. The recorded 36 holograms are reconstructed with angular spectrum enhanced by the iterative Gerchberg-Saxton procedure [40]. This algorithm is iterated five times, effectively eliminating the twin image noise, and upgrading the

signal-to-noise ratio. This algorithm is a well-established iterative phase retrieval technique that enables the reconstruction of the phase of a complex-valued wavefront from intensity measurements and Fourier transforms [40]. In this process, the Gabor hologram is initially propagated to the sample's plane, and only the reconstructed phase is retained, with the amplitude being discarded. The retrieved phase is then propagated back to the hologram's plane, where the amplitude is replaced by the square root of the recorded Gabor hologram. This complex field is subsequently propagated back to the sample's plane, and the procedure is repeated iteratively. In this study, this algorithm is specifically selected to minimize inherent noise, e.g., coming from the twin image effect [40]. The processing was performed on an Apple M3 chip, and the reconstruction of each hologram with the method took on average 14.8 s, with an uncertainty of 0.2 s, computed as the standard deviation of the measured times. From the reconstructed complex field, the intensity distributions are computed to provide the MM using Equations (2), the computation of this MM took on average 1.53 ± 0.15 s to compute. Fig. 2(a) shows the reconstructed negative pattern obtained using the proposed method (obtained from the PP configuration), while Fig. 2(b) displays the positive pattern (obtained from the PM configuration) corresponding to element 7.1 of the chart. The retardance is computed from Eq. (6) [18]. Fig. 2(c) depicts the retardance map in nanometers. The average retardance is measured from the vertical and horizontal patterns marked by the dashed lines in Fig. 2(c). The average retardance provided by the proposed method is 271 ± 14 nm, demonstrating a high degree of concordance with the expected result of 280 nm as specified by the manufacturer [41]. These results affirm the capability of the method to provide accurate and reliable quantitative measurements of polarization response.

For further validation purposes, a sample containing Calcium Oxalate crystals is utilized. Appendix B provides information on the experimental setup for this imaging sample. Here, the in-focus images (i.e., the distance z is set to zero in Fig. 1) are also recorded to corroborate the results. Fig. 3(a) and (b) display the intensity images obtained for the horizontal-horizontal (HH) and horizontal-vertical (HV) configurations in the image-plane setup. Including image-plane images serves as a validation step to ensure the accuracy and consistency of the MM retrieval method since no numerical reconstruction processes are required (i.e., fully optical plane-to-plane conjugation in a brightfield mode). This comparison assesses potential artifacts or deviations of the proposed technique from the reference method. In-line Gabor holograms are then acquired when the sample is repositioned by 10 mm. Panels (c) and (d) in Fig. 3 show the recorded defocused images obtained with the HH and HV configurations.

Fig. 4 quantitatively compares the polarization parameters, including linear dichroism (a), diattenuation (b), polarizance (c), and depolarization (d) for the Calcium Oxalate crystals. In the first columns of Fig. 4, the polarimetric measurements for the Mueller Bright Field setup (i.e., the image-plane configuration) are shown. The second and third columns show the results obtained with the proposed MG-HM method employing the classical and Gerchberg-Saxton angular spectrum reconstruction algorithms, respectively. The latter algorithm is iterated five times to reduce the twin image noise. The reconstruction time for this sample using the Gerchberg-Saxton algorithm is 5.15 ± 0.08 s meanwhile the classical angular spectrum is 1.20 ± 0.02 s. Overall, a high level of agreement between the results obtained by the image-plane configuration and the MG-HM method using the conventional angular spectrum is obtained, confirming the ability of the MG-HM method for precise quantitative polarization measurement. For quantitative analysis, the same crystal enclosed by a color rectangle in Fig. 4 has been selected to compare the results. The selected crystal is the one having a higher polarimetric response and a manual mask is created to measure the average linear dichroism, diattenuation, polarizance, and depolarization. The mean of the background noise selected in a blank region has also been measured; see the dashed rectangles in Fig. 4. Table 1 provides a summary of the quantitative values. It is clear that there is a high agreement between the results provided by the Mueller brightfield system and the MG-HM method using the classical angular spectrum formalism. On the other hand, the Gerchberg-Saxton reconstruction algorithm reduces the background noise compared to the classical angular spectrum algorithm, increasing the signal-to-noise ratio. Nonetheless, the results show that the retrieved polarimetric measurements using the Gerchberg-Saxton reconstruction algorithm present some minor reductions in the intensity signal, leading to discrepancies in some polarimetric measurements, such as the dichroism. Still, the significant enhancement in signal-to-noise ratio provided by the Gerchberg-Saxton reconstruction method reinforces its effectiveness for polarimetric analysis in complex and non-uniform sample scenarios where the structure of samples may need to be highlighted via background noise reduction.

4. Volumetric (multi-layer) mueller matrix retrieval

This section highlights the full potential of the proposed Gabor-Mueller method to facilitate the retrieval of multi-layer information from volumetric samples. It is essential to note that tissue specimens characterized by strong scattering have been deliberately excluded from the scope of this technique, given the prerequisite for the Gabor weak-scattering regime. Instead, our focus centers on axially sparse multi-plane samples exhibiting limited scattering. For this section, two volumetric specimens are prepared. The first specimen contains strategically positioned Calcium Oxalate crystals at the two faces of a microscope slide, as illustrated in Fig. 5(a). The second sample comprises two separate slides containing transparent polyethylene terephthalate (PET) plastic elements, as depicted in Fig. 5(b). Both imaging samples are volumetric samples characterized by purely numerical axial variations in polarimetric information, a feature that cannot be simultaneously recovered using conventional image-plane methods or other non-holographic/interferometric techniques.

In these experiments, each recorded hologram must be propagated at two distinct reconstruction distances, enabling the retrieval of information from both transverse planes of the crystals and PET

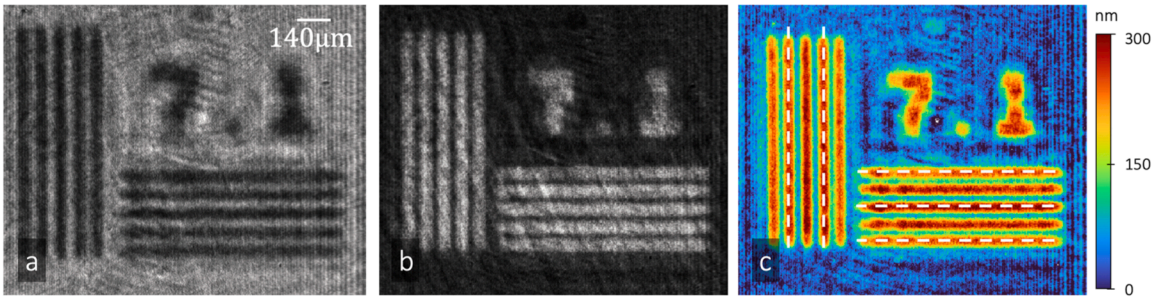

Fig. 2. Birefringent test target. (a) Reconstructed negative pattern. (b) Reconstructed positive pattern. (c) The retardance map measured with the proposed MG-HM technique.

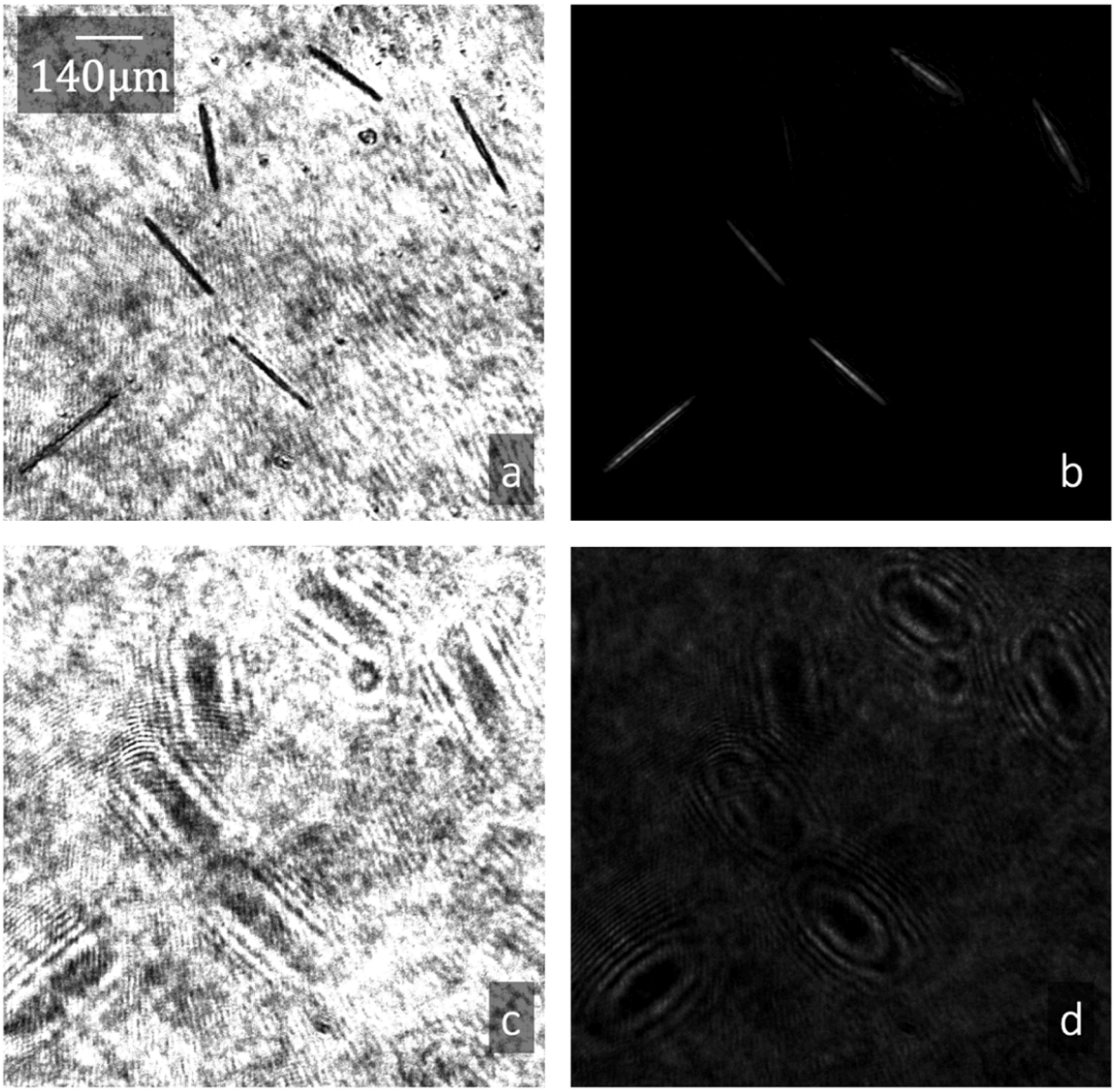

Fig. 3. Sample containing Calcium Oxalate crystals. Image-plane images ($z = 0$) for the HH configuration in (a) and for the HV configuration in (b). In-line Gabor holograms for the HH configuration in (c) and HV configuration in (d).

microplastics. Following the procedure outlined in Section 2, the complete MM of the sample is obtained at two separate transverse planes along the direction of light propagation. Fig. 6(a) and (b) illustrate the reconstructed intensity images of the crystals at distances 5.5 mm and 29.5 mm when the polarization states of the PSG and PSA systems are orthogonal (i.e., HV configuration). Fig. 6(c) and (d) show the reconstructed intensity images of the microplastics at distances 10.5 mm and 20.5 mm when the polarization states of the PSG and PSA systems are parallel (i.e., HH configuration). For both samples, the conventional angular spectrum reconstruction algorithm is used. More details of the experiment conditions are shown in Appendix B.

The Calcium Oxalate crystals present intrinsically linear dichroism, providing crucial insights into how these crystals differentially absorb linearly polarized light. Fig. 7 shows the reconstructed linear dichroism response of the crystal sample at the two different transverse planes, offering a comprehensive view of the dichroism properties of these crystals at different axial depths. The measured linear dichroism for each crystal at different transverse planes remains consistent with the experiments conducted in Section 3, with an average value of -0.6.

On the other side, Fig. 8 presents the linear dichroism (a), diattenuation (b), and depolarization (c) of the volumetric sample containing PET microplastics at the two different transverse planes. This visual contrast accentuates the out-of-focus nature of the other sample. The overall polarization response of the sample is high, as evidenced by the pronounced sample-to-background contrast in the measurements. This distinctive feature holds great significance as it can potentially reveal valuable component information within the sample, thereby enabling its characterization and detection—a pivotal aspect for various scientific and industrial applications regarding the recent rising concerns about microplastic effects [42,43]. This information underscores the method's capacity to capture complex polarimetric variations in volumetric specimens accurately. It offers valuable insights into the anisotropic properties of plastics across multiple contrast domains and enhances the understanding of their behavior under polarized light. These results vividly illustrate the method's proficiency in quantifying intricate polarimetric variations in volumetric specimens.

5. Conclusions

This work proposes an innovative approach that leverages the capabilities of in-line Gabor holography to extract precise polarization information from volumetric samples. The method integrates in-line

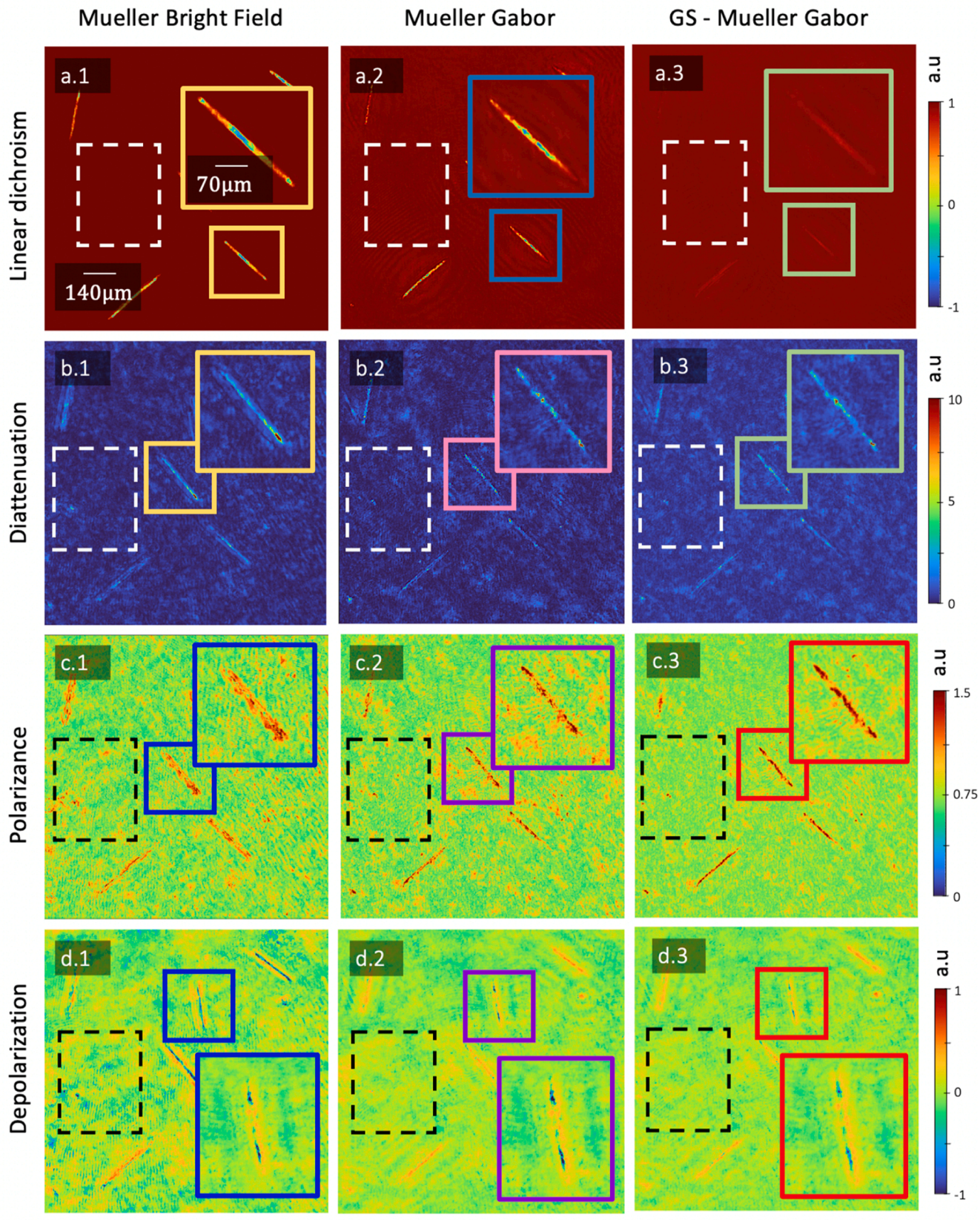

Fig. 4. Polarimetric properties of a sample containing Calcium Oxalate crystals. (a) Linear dichroism, (b) diattenuation, (c) polarizance, and (d) depolarization with (1) the reference Mueller Bright Field method, (2) the proposed MG-HM using the classical angular spectrum reconstruction method, and (3) the proposed MG-HM using the iterative Gerchberg-Saxton reconstruction algorithm.

Table 1
Quantitative results of the mueller bright field, mueller gabor, and the iterative gerchberg-saxton mueller gabor with a sample containing calcium oxalate crystals.

Polarimetric parameter	Mueller Bright Field		MG-HM		Iterative GS MG-HM	
	Crystal	Background noise	Crystal	Background noise	Crystal	Background noise
Linear dichroism	−0.6	0.001	−0.6	0.022	0.9	0.012
Diattenuation	3.0	0.242	2.9	0.207	2.4	0.149
Polarizance	1.0	0.153	1.0	0.152	0.9	0.108
Depolarization	−1.3	0.158	−1.2	0.082	−0.9	0.070

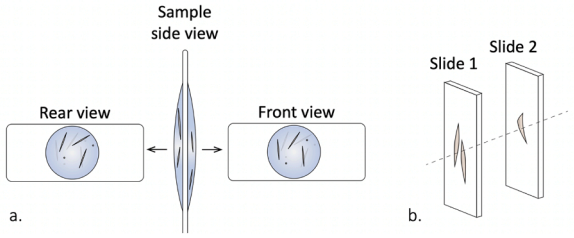

Fig. 5. (a) Setup of the volumetric sample containing Calcium Oxalate crystals. (b) Setup of the volumetric sample containing microplastics.

Gabor holography with a conventional polarimetric setup to recover the complete Mueller matrix of the sample. The robustness and accuracy of this technique have been demonstrated by imaging a calibrated birefringent test target. Additionally, the technique has been applied to extract the polarimetric parameters (i.e., dichroism, diattenuation, polarizance, and depolarization) of Calcium Oxalate crystals. The agreement between the polarimetric parameters obtained by the proposed method and the reference Mueller brightfield system is high, affirming the method's effectiveness in capturing the intricate polarization properties of complex samples. Finally, the full potential of the in-line Gabor holographic system is shown for volumetric samples of crystals and microplastics, demonstrating the capability of retrieving axial variations in polarimetric information – an achievement unattainable through conventional image-plane methods or non-holographic/interferometric systems. The visualization of such variations demonstrates the depth and sensitivity of the approach in uncovering the complex polarization characteristics of three-dimensional (3D) specimens. The method's applicability in examining 3D samples significantly broadens the horizons of analyzing complex materials and biological specimens using optical polarimetric methods across scientific and industrial domains. Future work will focus on optimizing the reconstruction algorithms, with a primary focus on noise reduction (in both software and hardware) and enhancing the sensitivity of polarimetric parameter recovery from the Mueller matrix. The current computational framework requires 36 holograms, not being suitable for dynamic imaging. We will investigate alternative computational methods to reduce the required number of recorded images, aiming to reduce the acquisition time per sample and make the proposed method suitable for real-time imaging. The importance of refining these technical aspects will further elevate the precision and reliability of the method to more applications.

CRediT authorship contribution statement

Maria J. Lopera: Conceptualization, Funding acquisition, Investigation, Methodology, Software, Validation, Visualization, Writing – original draft. **Maciej Trusiak:** Conceptualization, Funding acquisition, Supervision, Writing – review & editing. **Ana Doblas:** Conceptualization, Writing – review & editing. **Heidi Ottevaere:** Funding acquisition, Supervision, Writing – review & editing. **Carlos Trujillo:** Conceptualization, Funding acquisition, Supervision, Writing – original draft, Writing – review & editing.

Declaration of competing interest

The authors declare that they have no known competing financial interests or personal relationships that could have appeared to influence

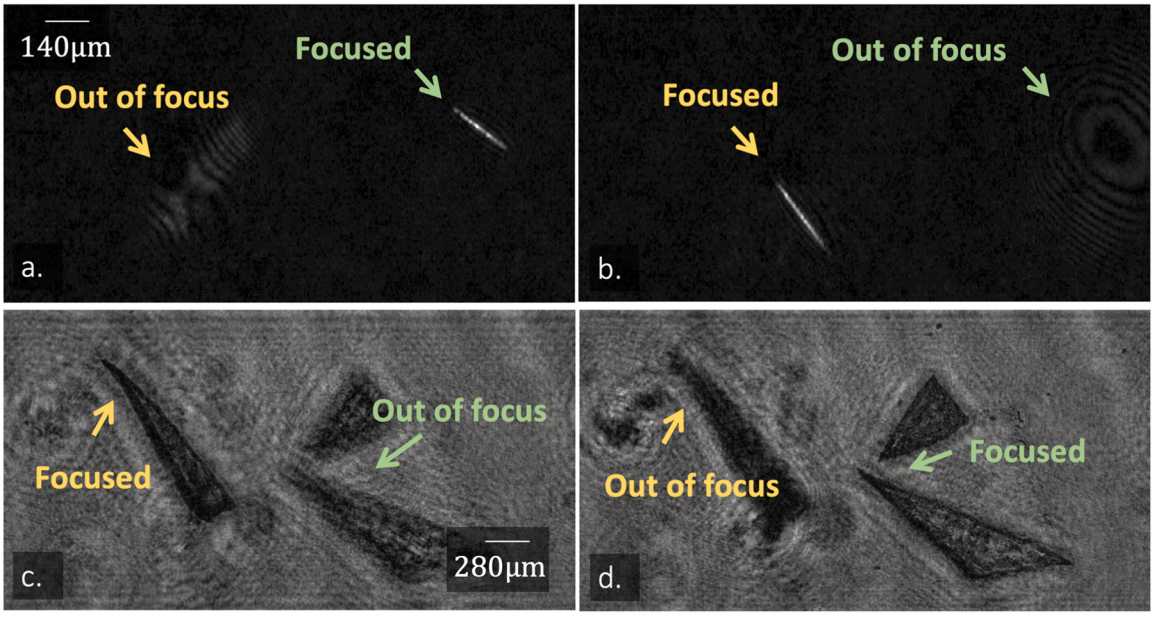

Fig. 6. Volumetric sample containing Calcium Oxalate crystals on both sides of the microscope slide. (a) The first crystal focused on the HV configuration. (b) The second crystal focused on the HV configuration. Volumetric sample containing microplastics focused on different distances (c) and (d) from the HH hologram.

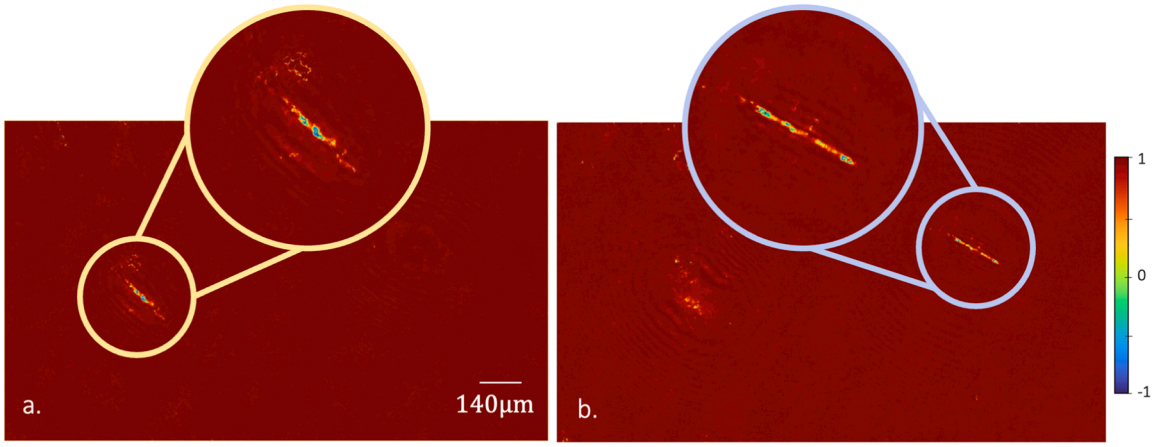

Fig. 7. Linear dichroism response of Calcium Oxalate crystals located at opposite faces of a microscope slide.

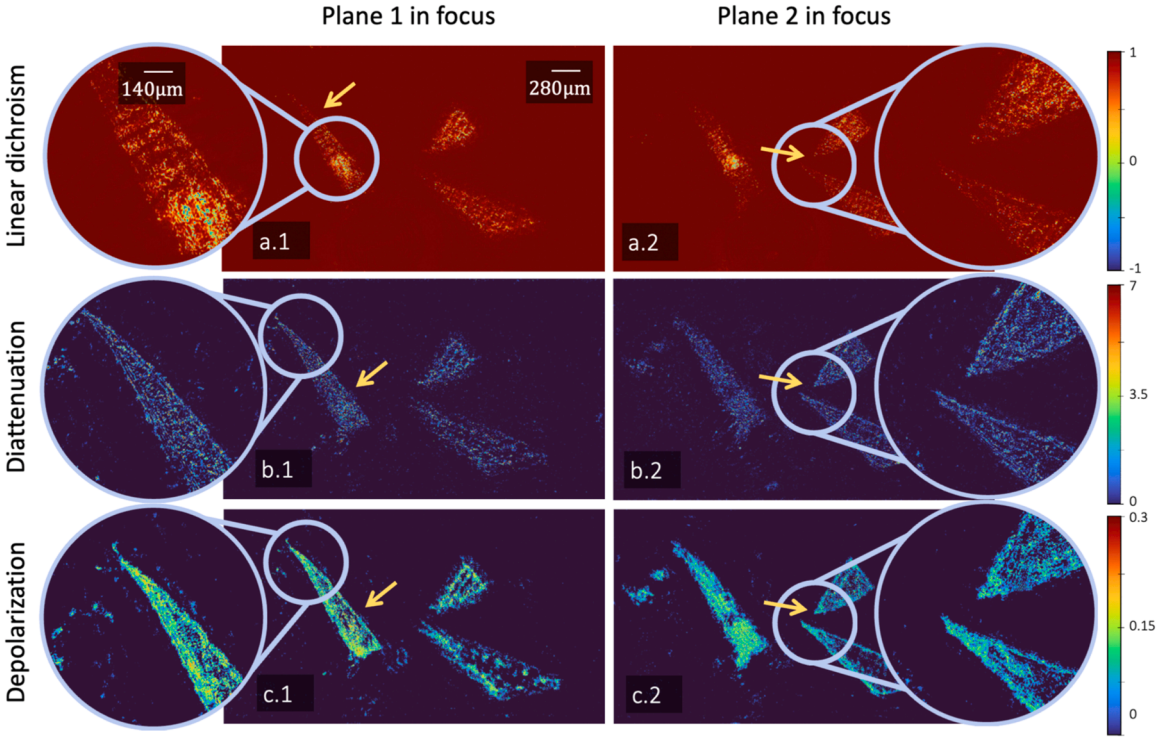

Fig. 8. Polarimetric properties of a sample containing PET plastics. (a) Linear dichroism, (b) diattenuation, (c) depolarization, at two different focal planes (1) and (2).

the work reported in this paper.

Data availability

Data will be made available on request.

Funding

This research has been funded by the National Science Center Poland (SONATA 2020/39/D/ST7/03236), the Ministerio de Ciencia Tecnología e Innovación under the call SGR 21, the Flemish Fund for Scientific Research (FWO) (11PGG24N), andthe Methusalem and Hercules foundations and the OZR of the Vrije Universiteit Brussel (VUB). The study was carried out on devices co-funded by the Warsaw University of Technology within the Excellence Initiative: Research University (IDUB) program. M.R. is supported by the Foundation for Polish Science (FNP start program) together as devices co-founded by Universidad EAFIT and the G8 Medellín Metropolitan Area universities funding "*Proyectos de I + D + i en el marco de la agenda regional I + D->i*".

Disclosures

During the preparation of this work, the author(s) used GPT-3.5 for spell check and grammar check. After using this tool, the author(s) reviewed and edited the content as needed and take(s) full responsibility for the content of the publication.

Acknowledgments

M. J. Lopera acknowledges the Flemish Fund for Scientific Research (FWO) for supporting her research (11PGG24N) and Minciencias

Research SGR21 Jovenes Investigadores program. M. J. Lopera and C. Trujillo acknowledge the support provided by Vicerrectoría de Ciencia, Tecnología e Innovación from Universidad EAFIT. Doblas acknowledges her funding from the National Science Foundation (2042563). The authors acknowledge the valuable help of Dr. Piotr Zdańkowski and Ph.D. candidates Piotr Arcab, Mikołaj Rogalski and Emilia Wdowiak.

Appendix A

To fully compute the Mueller matrix and a solvable linear system, 36 images should be acquired, changing the PSA and PSG to create the degenerate polarization states (H: horizontal, V: vertical, P: +45, M: −45, R: right circular, L: left circular).

For the case of this study, a horizontally polarized light is employed. Based on that, the angles needed to set the PSA and PSG in all configurations for the PSA and PSG are described as follows: (modified from [15])

Notation	Orientation angles (°) PSG HWP	QWP	PSA QWP	LP	Notation	Orientation angles (°) PSG HWP	QWP	PSA QWP	LP
HV	0	0	90	90	PV	22.5	45	90	90
HH	0	0	90	0	PH	22.5	45	90	0
HP	0	0	−45	45	PP	22.5	45	−45	45
HM	0	0	−45	−45	PM	22.5	45	−45	−45
HR	0	0	0	−45	PR	22.5	45	0	−45
HL	0	0	0	45	PL	22.5	45	0	45
VV	45	90	90	90	RV	22.5	90	90	90
VH	45	90	90	0	RH	22.5	90	90	0
VP	45	90	−45	45	RP	22.5	90	−45	45
VM	45	90	−45	−45	RM	22.5	90	−45	−45
VR	45	90	0	−45	RR	22.5	90	0	−45
VL	45	90	0	45	RL	22.5	90	0	45
MV	−22.5	−45	90	90	LV	45	90	90	90
MH	−22.5	−45	90	0	LH	45	90	90	0
MP	−22.5	−45	−45	45	LP	45	90	−45	45
MM	−22.5	−45	−45	−45	LM	45	90	−45	−45
MR	−22.5	−45	0	−45	LR	45	90	0	−45
ML	−22.5	−45	0	45	LL	45	90	0	45

In the case of different incident light, the configurations can be easily computed by the Stokes calculus, considering that the general matrix equation for a linear retarder is given by:

$$\begin{vmatrix} 1 & 0 & 0 & 0 \\ 0 & \cos^2(2\theta)+\sin^2(2\theta)\cos(\delta) & \cos(2\theta)\sin(2\theta)\,(1-\cos(\delta)) & \sin(2\theta)\sin(\delta) \\ 0 & \cos(2\theta)\sin(2\theta)\,(1-\cos(\delta)) & \cos^2(2\theta)\cos(\delta)+\sin^2(2\theta) & -\cos(2\theta)\sin(\delta) \\ 0 & \sin(2\theta)\sin(\delta) & \cos(2\theta)\sin(\delta) & \cos(\delta) \end{vmatrix}$$

And the general matrix equation for a linear polarizer is given by:

$$1/2 \begin{vmatrix} 1 & \cos(2\theta) & 0 & 0 \\ \cos(2\theta) & \cos^2(2\theta) & \cos(2\theta)\sin(2\theta) & 0 \\ \sin(2\theta) & \cos(2\theta)\sin(2\theta) & \sin^2(2\theta) & 0 \\ 0 & 0 & 0 & 0 \end{vmatrix}$$

As the PSG is composed of a half-wave plate followed by a quarter waveplate, their retardance (δ) is replaced on the linear retarder matrix equation, and the PSG matrix is computed by multiplying the following matrices.

$$\mathrm{PSG\_HWP} = \begin{vmatrix} 1 & 0 & 0 & 0 \\ 0 & \cos^2(2\theta)-\sin^2(2\theta) & 2\cos(2\theta)\sin(2\theta) & 0 \\ 0 & 2\cos(2\theta)\sin(2\theta) & -\cos^2(2\theta)+\sin^2(2\theta) & 0 \\ 0 & 0 & 0 & -1 \end{vmatrix}$$

$$\mathrm{PSG\_QWP} = \begin{vmatrix} 1 & 0 & 0 & 0 \\ 0 & \cos^2(2\theta) & \cos(2\theta)\sin(2\theta) & \sin(2\theta) \\ 0 & \cos(2\theta)\sin(2\theta) & \sin^2(2\theta) & -\cos(2\theta) \\ 0 & \sin(2\theta) & \cos(2\theta) & 0 \end{vmatrix}$$

The same procedure can be done for the PSA, obtaining the following matrices:

$$\text{PSA\_QWP} = \begin{vmatrix} 1 & 0 & 0 & 0 \\ 0 & \cos^2(2\theta) & \cos(2\theta)\sin(2\theta) & \sin(2\theta) \\ 0 & \cos(2\theta)\sin(2\theta) & \sin^2(2\theta) & -\cos(2\theta) \\ 0 & \sin(2\theta) & \cos(2\theta) & 0 \end{vmatrix}$$

$$\text{PSA\_LP} = 1/2 \begin{vmatrix} 1 & \cos(2\theta) & 0 & 0 \\ \cos(2\theta) & \cos^2(2\theta) & \cos(2\theta)\sin(2\theta) & 0 \\ \sin(2\theta) & \cos(2\theta)\sin(2\theta) & \sin^2(2\theta) & 0 \\ 0 & 0 & 0 & 0 \end{vmatrix}$$

The Mueller matrix contains the overall polarimetric information of a sample, providing its diattenuation (M_D), polarizance (M_Δ) and retardance (M_R). Each of these properties can be independently estimated after the Mueller matrix is decomposed, as expressed as follows:

$\boldsymbol{M} = \boldsymbol{M_\Delta}\cdot\boldsymbol{M_R}\cdot\boldsymbol{M_D}$.

The decomposition can be computed with the polar approach as described by Lu S-Y et.al [18]. Firstly, the diattenuation $\boldsymbol{M_D}$ can be calculated from

$$\boldsymbol{M_D} = \begin{bmatrix} 1 & \boldsymbol{D}^T \\ \boldsymbol{D} & \boldsymbol{m_D} \end{bmatrix}$$

where

$$\boldsymbol{m_D} = \sqrt{1-D^2}\boldsymbol{I} + \left(1-\sqrt{1-D^2}\right)\widehat{D}\widehat{D}^T$$

and

$$\boldsymbol{D} = \frac{1}{m_{00}}\begin{bmatrix} m_{01} \\ m_{02} \\ m_{03} \end{bmatrix}.$$

In the above equations $\boldsymbol{D}$ is the diattenuation vector extracted directly from the Mueller matrix components, D is the norm of the diattenuation vector, $\widehat{D}\widehat{D}^T$ constructs the unit diattenuation vector, and $\boldsymbol{m_D}$ is a 3×3 submatrix constructed in terms of the $\boldsymbol{D}$ vector and the identity matrix **(*I*).**

Once the diattenuation matrix is obtained, a secondary matrix (***M'),*** which only depends on the polarizance and retardance information of the sample, is obtained by multiplying the Mueller matrix (***M)*** and the transpose of the diattenuation matrix (***D***). Being $x^T$the transpose of the matrix $\boldsymbol{x}$.

$$\boldsymbol{M}' = \boldsymbol{M}\cdot\boldsymbol{M_D^T} = \boldsymbol{M_\Delta}\cdot\boldsymbol{M_R}.$$

Considering the following polar decomposition for the polarizance and retardance matrices, the elements of the secondary matrix can be expressed as

$$\boldsymbol{M}' = \begin{bmatrix} 1 & 0^T \\ \boldsymbol{P_\Delta} & \boldsymbol{m_\Delta} \end{bmatrix}\begin{bmatrix} 1 & 0^T \\ 0 & \boldsymbol{m_R} \end{bmatrix} = \begin{bmatrix} 1 & 0^T \\ \boldsymbol{P_\Delta} & \boldsymbol{m}' \end{bmatrix}$$

In the secondary matrix, $\boldsymbol{0}$ is a zero-column vector. The elements of the polarizance matrix $\boldsymbol{M_\Delta}$ can be determined as follows

$$\boldsymbol{P_\Delta} = \frac{\boldsymbol{P} - \boldsymbol{m}\cdot\boldsymbol{D}}{1-D^2}$$

being

$$\boldsymbol{P} = \frac{1}{m_{00}}\begin{bmatrix} m_{10} \\ m_{20} \\ m_{30} \end{bmatrix}$$

And $\boldsymbol{m}$ the 3×3 submatrix of the Mueller matrix.

The $\boldsymbol{m_\Delta}$ matrix is calculated by

$$m_\Delta = \pm\left[m'm'^T + \left(\sqrt{\lambda_1\lambda_2} + \sqrt{\lambda_2\lambda_3} + \sqrt{\lambda_3\lambda_1}\right)I\right]^{-1} \times \left[\left(\sqrt{\lambda_1} + \sqrt{\lambda_2} + \sqrt{\lambda_3}\right)m'm'^T + \left(\sqrt{\lambda_1\lambda_2\lambda_3}\right)I\right]$$

where $\lambda_1,\ \lambda_2,\ \lambda_3$ are the eigenvalues of the matrix $m'\cdot m'^T$, in which m' is the submatrix of the secondary matrix (based on the decomposition $m' = m_\Delta\cdot m_R$**).**

Finally, the retardance matrix $\boldsymbol{M_R}$ is defined by the multiplication between the inverse of the polarizance matrix $\boldsymbol{M_\Delta^{-1}}$ and the secondary matrix $\boldsymbol{M}'$

$$\boldsymbol{M_R} = \boldsymbol{M_\Delta^{-1}}\cdot\boldsymbol{M}' = \begin{bmatrix} 1 & 0^T \\ 0 & \boldsymbol{m_R} \end{bmatrix}$$

Appendix B

The details of the setup used in each of the validation experiments are provided in the following table.

Sample	λ (nm)	Pixel pitch (μm)	Mag.	Lateral Resolution (μm)	Rec. distance (mm)	Rec. algorithm	Rec. time (s)
Birefringent target	561s	2.74	1 ×	2.74	7	Gerchberg-Saxton AS	14.8 ± 0.2
Plane Calcium Oxalate	532	3.75	10 ×	1.64	10.5	Angular Spectrum, Gerchberg-Saxton AS	5.15 ± 0.08 1.20 ± 0.02
Volumetric Calcium Oxalate	532	3.75	10 ×	1.64	5.5, 29.5	Angular Spectrum	0.83 ± 0.02
Volumetric Plastic	532	2.74	4 ×	1.33	10.5, 20.5	Angular Spectrum	14.8 ± 0.2

Depth of field of the used microscope objectives:

Magnification	Numerical aperture	Depth of field
4 ×	0.20	45 μm
10 ×	0.25	13 μm

References

[1] Hogan BT, Ushenko VA, Syvokorovskaya AV, Dubolazov AV, Vanchulyak OY, Ushenko AG, et al. 3D Mueller matrix reconstruction of the optical anisotropy parameters of myocardial histopathology tissue samples. Front Phys 2021;9:737866. https://doi.org/10.3389/FPHY.2021.737866/BIBTEX.

[2] He H, Liao R, Zeng N, Li P, Chen Z, Liu X, et al. Mueller matrix polarimetry-An emerging new tool for characterizing the microstructural feature of complex biological specimen. J Lightwave Technol 2019;37:2534–48. https://doi.org/10.1109/JLT.2018.2868845.

[3] Byrum JR, Perez-Bermejo JA, Leonetti MD, Ivanov IE, Mehta SB, Kim JYS, et al. Correlative imaging of the spatio-angular dynamics of biological systems with multimodal instant polarization microscope. Biomed Opt Express 2022;13(5):3102–19. https://doi.org/10.1364/BOE.455770.

[4] Gratiet A Le, Sheppard C.J.R., Diaspro A Biological Imaging Through Optical Mueller Matrix Scanning Microscopy. Optical Polarimetric Modalities for Biomedical Research. Biological and Medical Physics, Biomedical Engineering 2023;101–123. doi:10.1007/978-3-031-31852-8_5. Springer.

[5] Sampaio P, Lopez-Antuña M, Storni F, Wicht J, Sökeland G, Wartenberg M, et al. Müller matrix polarimetry for pancreatic tissue characterization. Sci Rep 2023;13(1):1–9. https://doi.org/10.1038/s41598-023-43195-7.

[6] Khan S, Qadir M, Khalid A, Ashraf S, Ahmad I. Characterization of cervical tissue using Mueller matrix polarimetry. Lasers Med Sci 2023;38:1–11. https://doi.org/10.1007/S10103-023-03712-6/FIGURES/6.

[7] Tuchin VV. Polarized light interaction with tissues. J Biomed Opt 2016;21:071114. https://doi.org/10.1117/1.jbo.21.7.071114.

[8] Agrawal GP. Chapter 6. Polarization effects. Nonlinear Fiber Optics; 2019. p. 189–244. https://doi.org/10.1016/b978-0-12-817042-7.00013-0. In: Inc. E, editor2019th editor.

[9] Dubolazov OV, Karachevtsev AO, Ushenko VA. Two wavelength Mueller matrix reconstruction of blood plasma films polycrystalline structure in diagnostics of breast cancer. Appl Opt 2014;53(10):B128–39. https://doi.org/10.1364/AO.53.00B128.

[10] Ushenko YA, Koval GD, Ushenko AG, Dubolazov OV, Ushenko VA, Novakovskaia OY. Mueller-matrix of laser-induced autofluorescence of polycrystalline films of dried peritoneal fluid in diagnostics of endometriosis. Journal of Biomedical Optics 2016;21(7):071116. https://doi.org/10.1117/1.JBO.21.7.071116.

[11] Ghosh N, Wood MFG, hong Li S, Weisel RD, Wilson BC, Li RK, et al. Mueller matrix decomposition for polarized light assessment of biological tissues. J Biophotonics 2009;2:145–56. https://doi.org/10.1002/JBIO.200810040.

[12] Gou J, Shen TH, Bao P, Ramos Angulo JL, Evans SD. A stokes polarimetric light microscopy view of liquid crystal droplets. Sci Rep 2021;11(1):1–9. https://doi.org/10.1038/s41598-021-95674-4.

[13] Pezzaniti JL, Chipman RA. Mueller matrix imaging polarimetry 1995;34:1558–68. https://doi.org/10.1117/12.206161.

[14] Coppola G, Ferrara MA. Polarization-sensitive digital holographic imaging for characterization of microscopic samples: recent advances and perspectives. Applied Sciences (Switzerland) 2020;10. https://doi.org/10.3390/app10134520.

[15] Obando-Vasquez S, Doblas A, Trujillo C. Apparatus and method to recover the Mueller matrix in bright-field microscopy. Am J Phys 2022;90:702–14. https://doi.org/10.1119/5.0081673.

[16] Zayko S, Kfir O, Ropers C. Polarization-sensitive coherent diffractive imaging using HHG. Topics in Applied Physics 2020;134:501–22. https://doi.org/10.1007/978-3-030-34413-9_18. Springer.

[17] Collett E. Field guide to polarization. Washington: SPIE Field Guides, SPIE Press; 2005. https://doi.org/10.1117/3.626141. Volume FG0.

[18] Lu S-Y, Chipman RA, Lu S-Y, Chipman RA. Interpretation of Mueller matrices based on polar decomposition. J. Opt. Soc. Am. A 1996;13:1106–13. https://doi.org/10.1264/JOSAA.12.001106.

[19] Dubreuil M, Gratiet A Le, Rivet S, Le Grand Y. Scanning Mueller polarimetric microscopy. Opt Lett 2016;41(18):4336–9. https://doi.org/10.1364/OL.41.004336.

[20] Bargmann CI, Gladfelter AS, McQuilken M, Heintzmann R, Ilic R, Larsch J, et al. MultiFocus Polarization Microscope (MF-PolScope) for 3D polarization imaging of up to 25 focal planes simultaneously. Opt Express 2015;23(6):7734–54. https://doi.org/10.1364/OE.23.007734.

[21] Bosch S, Javidi B, Carnicer A. Mueller matrix polarimetry with 3D integral imaging. Opt Express 2019;27(8):11525–36. https://doi.org/10.1364/OE.27.011525.

[22] Beghuin D, Depeursinge C, Dahlgren P, Marquet P, Colomb T, Cuche E. Polarization imaging by use of digital holography. Appl Opt 2002;41(1):27–37. https://doi.org/10.1364/AO.41.000027.

[23] Colomb T, Dürr F, Cuche E, Marquet P, Limberger HG, Salathé RP, et al. Polarization microscopy by use of digital holography: application to optical-fiber birefringence measurements. Appl Opt 2005;44:4461–9. https://doi.org/10.1364/AO.44.004461.

[24] Palacios F, Font O, Palacios G, Ricardo J, Escobedo M, Ferreira L, et al. Phase and polarization contrast methods by use of digital holographic microscopy: applications to different types of biological samples. holography - Basic Principles and contemporary applications. InTech; 2013. https://doi.org/10.5772/54022.

[25] Gao M, Yang P, McKee D, Kattawar GW. Mueller matrix holographic method for small particle characterization: theory and numerical studies. Appl Opt 2013;52(21):5289–96. https://doi.org/10.1364/AO.52.005289.

[26] Nomura T, Kobata T. Mueller matrix imaging by use of digital holography. SPIE Proceedings: Optical Systems and Modern Optoelectronic Instruments 2015;9618:52–8. https://doi.org/10.1117/12.2191480.

[27] Abbasian V, Abbasian V, Moradi A-R, Moradi A-R. Microsphere-assisted super-resolved Mueller matrix microscopy. Opt Lett 2020;45(15):4336–9. https://doi.org/10.1364/OL.395735.

[28] Zheng J, Chen Z, Ushenko O, Dubolazov OV, Olar O, Gavrilyak M, et al. Mueller-matrix microscopy of diffuse layers of polyvinyl acetate with digital holographic reconstruction of layer-by-layer depolarization. maps 2021;12126:668–74. https://doi.org/10.1117/12.2617049.

[29] GABOR D. A new microscopic principle. Nature 1948;161:777. https://doi.org/10.1038/161777a0.

[30] Trindade K, Micó V, Picazo-Bueno JÁ. Phase imaging microscopy under the Gabor regime in a minimally modified regular bright-field microscope. Opt Express 2021;29(26):42738–50. https://doi.org/10.1364/OE.444884.

[31] Garcia-Sucerquia J, Xu W, Jericho SK, Klages P, Jericho MH, Kreuzer HJ. Digital in-line holographic microscopy. Appl Opt 2006;45:836–50. https://doi.org/10.1364/AO.45.000836.

[32] Wang P-H, Lin W-T, Zhai X, Luo Y, Singh VR, Tsai J-C, et al. In-line digital holographic imaging in volume holographic microscopy. Opt Lett 2015;40(23):5542–5. https://doi.org/10.1364/OL.40.005542.

[33] Molony KM, Hennelly BM, Kelly DP, Naughton TJ. Reconstruction algorithms applied to in-line Gabor digital holographic microscopy. Opt Commun 2010;283:903–9. https://doi.org/10.1016/J.OPTCOM.2009.11.012.

[34] Galdón L, Garcia-Sucerquia J, Saavedra G, Martínez-Corral M, Sánchez-Ortiga E, Sánchez-Ortiga E. Resolution limit in opto-digital systems revisited. Opt Express 2023;31(2):2000–12. https://doi.org/10.1364/OE.479458.

[35] Kreis T. Handbook of Holographic Interferometry: optical and Digital Methods. Handbook of Holographic Interferometry: Optical and Digital Methods 2005:1–542. https://doi.org/10.1002/3527604154.

[36] Kim MK. Digital holographic microscopy. Springer Ser Opt Sci 2011;162:149–90. https://doi.org/10.1007/978-1-4419-7793-9_11/FIGURES/34_11.
[37] Goodman JW. Introduction to fourier optics. Greenwood Village: Roberst & Company Publishers; 2005.
[38] Mendlovic D, Zalevsky Z, Konforti N. Computation considerations and fast algorithms for calculating the diffraction integral. J Mod Opt 1997;44:407–14. https://doi.org/10.1080/09500349708241880.
[39] Sabbah S, Shashar N. Polarization contrast of zooplankton: a model for polarization-based sighting distance. Vision Res 2006;46:444–56. https://doi.org/10.1016/J.VISRES.2005.05.017.
[40] Gao Y, Cao L, Gao Y, Cao L. Iterative projection meets sparsity regularization: towards practical single-shot quantitative phase imaging with in-line holography. Light: Advanced Manufacturing 2023;4:37–53. https://doi.org/10.37188/LAM.2023.006.
[41] Thorlabs. Thorlabs NBS 1963A Birefringent Resolution Target 2023. https://www.thorlabs.com/newgrouppage9.cfm?objectgroup_id=4338&pn=R2L2S1B (accessed September 18, 2023).
[42] Li Y, Zhu Y, Huang J, Zhang Y, Lam EY. Polarization Holographic Imaging for High-throughput Microplastic Analysis. Optica Imaging Congress, Optica Publishing Group; 2023.
[43] Bianco V, Memmolo P, Carcagnì P, Merola F, Paturzo M, Distante C, et al. Microplastic Identification via Holographic Imaging and Machine Learning. Advanced Intelligent Systems 2020;2:1900153. https://doi.org/10.1002/AISY.201900153.